

Nebular spectra of kilonovae with detailed recombination rates - I. Light *r*-process composition

SMARANIKA BANERJEE ¹, ANDERS JERKSTRAND ¹, NIGEL BADNELL,² QUENTIN POGNAN ³, NIAMH FERGUSON ², AND
JON GRUMER ⁴

¹*The Oskar Klein Centre, Department of Astronomy, Stockholm University, AlbaNova, SE-10691 Stockholm, Sweden*

²*Department of Physics, University of Strathclyde, Glasgow G4 0NG, United Kingdom.*

³*Max-Planck-Institute for Gravitational Physics (Albert Einstein Institute), Am Mühlenberg 1, Potsdam-Golm, 14476, Germany*

⁴*Theoretical Astrophysics, Department of Physics and Astronomy, Uppsala University, Box 516, SE-751 20 Uppsala, Sweden*

(Received; Revised; Accepted February 6, 2025)

ABSTRACT

To investigate spectra of kilonovae in the NLTE phase ($t \gtrsim 1$ week), we perform atomic calculations for dielectronic (DR) and radiative (RR) recombination rates for the light *r*-process elements Se ($Z = 34$), Rb ($Z = 37$), Sr ($Z = 38$), Y ($Z = 39$), and Zr ($Z = 40$) using the HULLAC code. For the different elements, our results for the total rate coefficients for recombining from the ionization states of II to I, III to II, and IV to III vary between $10^{-13} - 10^{-9} \text{ cm}^3 \text{ s}^{-1}$, $10^{-12} - 10^{-10} \text{ cm}^3 \text{ s}^{-1}$, and $10^{-13} - 10^{-10} \text{ cm}^3 \text{ s}^{-1}$, respectively, at a temperature of $T = 10,000$ K. We also provide fits to the ground state photoionization cross sections of the various ions, finding larger and more slowly declining values with energy in comparison to the hydrogenic approximation. Using this new atomic data, we study the impact on kilonova model spectra at phases of $t = 10$ days and $t = 25$ days using the spectral synthesis code SUMO. Compared to models using the previous treatment of recombination as a constant rate, the new models show significant changes in ionization and temperature, and correspondingly, in emergent spectra. With the new rates, we find that Zr ($Z = 40$) plays a yet more dominant role in kilonova spectra for light *r*-process compositions. Further, we show that previously predicted mid-infrared (e.g. [Se III] $4.55 \mu\text{m}$) and optical (e.g. [Rb I] $7802, 7949 \text{ \AA}$) lines disappear in the new model. Instead a strong [Se I] line is seen to be emerging at $\lambda = 5.03 \mu\text{m}$. These results demonstrate the importance of considering the detailed microphysics for modelling and interpreting the late-time kilonova spectra.

Keywords: Neutron star, atomic calculation, kilonova, spectra, radiative transfer

1. INTRODUCTION

It has long been hypothesized that *r*-process elements are synthesized in neutron star mergers (e.g., Lattimer & Schramm 1974; Eichler et al. 1989; Freiburghaus et al. 1999; Korobkin et al. 2012; Wanajo et al. 2014). The radioactive decays of the freshly synthesized heavy elements give rise to a transient at ultraviolet, optical, and near-infrared wavelengths called a kilonova (e.g., Li & Paczyński 1998; Kulkarni 2005; Metzger et al. 2010). The first kilonova, AT2017gfo (e.g., Coulter et al. 2017; Yang et al. 2017; Valenti et al. 2017; Cowperthwaite et al. 2017; Smartt et al. 2017; Drout et al. 2017; Ut-

sumi et al. 2017) was observed following the gravitational wave event GW170817 (Abbott et al. 2017), opening up a new avenue of multi-messenger astrophysics.

Several efforts have been made to interpret the light curves of the kilonova observed (AT2017gfo) starting from as early as an hour (e.g., Kasen et al. 2017; Tanaka et al. 2017; Shibata et al. 2017; Perego et al. 2017; Ross-wog et al. 2018; Kawaguchi et al. 2018; Banerjee et al. 2020, 2022, 2024), confirming the prediction about the synthesis of *r*-process elements in neutron star mergers. Furthermore, the modelling of AT2017gfo spectra has indicated signatures of several heavy elements; a few of the examples include Sr ($Z = 38$, Watson et al. 2019) and Ce ($Z = 58$, Domoto et al. 2022).

These mentioned works are based on the modelling and interpretation of the early, photospheric-phase spec-

tra. At this phase, the bulk of the ejecta is optically thick, and the kilonova is in the diffusion phase. In this phase, an assumption of local thermal equilibrium (LTE) is used to model the kilonova light curves and spectra. However, after about a week or so, the diffusion phase ends and the kilonova enters its tail phase. The assumption of equilibrium breaks down and photospheric scattering lines now start to give way to emission lines, even though there is still significant line opacity and associated fluorescence (Pognan et al. 2023). The work on this phase requires considering non-LTE (NLTE) and has begun more recently (e.g., Hotokezaka et al. 2021, 2022; Pognan et al. 2022a, 2023; Hotokezaka et al. 2023). The NLTE spectral modelling of kilonovae has already indicated a few elemental signatures, such as Se ($Z = 34$, Hotokezaka et al. 2022), Te ($Z = 34$, Hotokezaka et al. 2023), and Rb ($Z = 37$, Pognan et al. 2023).

To model kilonovae in the NLTE phase, the ionization and excitation populations need to be determined by solving rate equations (e.g., Hotokezaka et al. 2022). Such calculations require the rates and the cross-sections of different processes for the r -process elements. Such data include: (1) Energy levels and spontaneous radiative transition rates (A-values), (2) thermal collisional bound-bound rates, (3) non-thermal collisional bound-free cross-sections, (4) photo-ionization (PI) cross-sections, and (5) (thermal) recombination rates.

The availability of experimental or even theoretical calculations for such atomic data is limited for the r -process elements, and previous works to model KN spectra have often involved new calculations of the needed atomic data. For example, Hotokezaka et al. (2021) calculate the energy levels and A-values by using GRASP2K (Froese Fischer et al. 2019) for Nd ($Z=60$) at ionization states II - IV. In Pognan et al. (2023), energy levels and A-values are calculated with the Flexible Atomic Code (FAC, Gu 2008) for the elements Ga ($Z = 31$) - U ($Z = 92$) for ionization states I - IV.

In the nebular phase, the ionization occurs mainly via non-thermal collisions by the high-energy electrons created in the downscattering cascade of radioactive decay particles, and photoionizations (PI). Recombination proceeds via direct radiative (RR) and resonant dielectronic recombination (DR) processes. Hence, DR and RR rates, as well as PI cross-sections, are crucial for accurate modelling of the ionization state in the NLTE phase. Such recombination rates and PI cross-sections for r -process elements, especially at the low ionization states applicable for kilonova, are scarce, with only a few existing works. For example, Preval et al. (2019) calculate the recombination rate coefficients of the lower

ionized W ($Z = 74$, ionization states II to XIV). Furthermore, Sterling & Witthoeft (2011) and Sterling (2011) calculate the recombination and PI cross-sections of low charged Se ($Z = 34$) and Kr ($Z = 36$) ions (up to ionization states of VI). However, such sparse works are not enough to calculate accurate spectra of kilonova at nebular phase.

In the work of Pognan et al. (2023), they use a (temperature-independent) constant total recombination rate of $10^{-11} \text{ cm}^3 \text{ s}^{-1}$. Additionally, a simplistic hydrogenic treatment for PI cross-sections is used. Conversely, Hotokezaka et al. (2021) perform atomic calculations to determine DR rates only for Nd ions (stages II - IV) and follow the analytical treatment of Axelrod (1980) for RR rates.

In this work, we perform atomic calculations to determine the total recombination rate coefficients, including both DR and RR contributions, for several r -process elements. We also compute the PI cross-sections as the inverse process of RR (through the Milne relations). Since calculation of atomic rates for all r -process elements is a very large endeavor, we focus initially on a subset of light r -process elements: Se ($Z = 34$), Rb ($Z = 37$), Sr ($Z = 38$), Y ($Z = 39$), and Zr ($Z = 40$). These elements are chosen because they have demonstrated potential to produce strong spectral signatures in kilonova nebula (Hotokezaka et al. 2022; Gillanders et al. 2022; Pognan et al. 2023). We consider recombination to I - III ions (neutral to doubly ionized), as these are most relevant during the nebular phase (e.g., Pognan et al. 2023). Using this new data, we then study how kilonova NLTE models are impacted using the SUMO spectral synthesis code.

The paper is structured as follows. We discuss the details of the atomic data requirements and our method of calculation in Section 2. We provide the results for our atomic calculations in Section 3. We discuss our spectral synthesis results in Section 4. We finally summarize our conclusions in Section 5.

2. ATOMIC DATA FOR NEBULAR SPECTRA

2.1. HULLAC

For the atomic calculations, we use HULLAC (Hebrew University Lawrence Livermore Atomic Code, Bar-Shalom et al. 2001). HULLAC is a set of programs that uses the same set of wavefunctions to calculate the different processes with the same level of accuracy. The performance of HULLAC is focused on the ionized heavy elements with several open shells. This is one of the major reasons for using this code since the main purpose of this work is to perform atomic calculations for such ions. The theoretical framework is outlined in previous works

Table 1. Configurations used to perform atomic calculations. The bold configurations are used as ground configurations and optimization.

Element	Ion	Configurations
Se	I	4s²4p⁴ , 4s²4p³4d , 4s²4p³4f , 4s ² 4p ³ nl ($n \leq 10$ for $l \leq 3$, $n \leq 8$ for $l \leq 5$), 4s ² 4p ² 4d5p, 4s4p ⁵ , 4s4p ⁴ 5p, 4s4p ³ 5p ² , 4p ⁶
Se	II	4s²4p³ , 4s4p⁴ , 4s ² 4p ² nl (for $l \leq 2$, $n \leq 9$, $2 < l \leq 5$, $n \leq 7$)
Se	III	4s²4p² , 4s4p³ , 4s ² 4pnl ($n \leq 13$ for $l = 0$, $n \leq 11$ for $0 < l \leq 2$, $n \leq 9$ for $2 < l \leq 4$, $n \leq 10$ for $l = 5$)
Se	IV	4s²4p , 4s ² nl ($n \leq 9$ for $0 < l \leq 2$, $n \leq 7$ for $2 < l \leq 5$), 4p ³ , 4s4p ²
Rb	I	4p⁶5s , 4p⁶5p , 4p⁶4d , 4p⁶4f , 4p ⁶ nl ($n \leq 10$ for $l \leq 2$, $n \leq 8$ for $l \leq 5$), 4p ⁵ 5s ² , 4p ⁵ 5snl ($n \leq 7$ for $l \leq 2$, $n \leq 5$ for $l = 3$)
Rb	II	4p⁶ , 4p⁵5s , 4p⁵5p , 4p⁵4d , 4p⁵4f , 4p ⁵ nl ($n \leq 10$ for $l \leq 2$, $n \leq 8$ for $l \leq 5$)
Rb	III	4p⁵ , 4p⁴4d , 4p⁴5p , 4p⁴5s , 4p⁴4f , 4p ⁴ nl ($n \leq 10$ for $l \leq 2$, $n \leq 8$ for $l \leq 5$)
Rb	IV	4p⁴ , 4p ³ nl ($n \leq 10$ for $l \leq 2$, $n \leq 8$ for $l \leq 5$)
Sr	I	5s² , 5s5p , 5s4d , 5snl ($n \leq 10$ for $l \leq 2$, $n \leq 8$ for $l \leq 5$), 4dnl ($n \leq 10$ for $l \leq 1$, $n \leq 8$ for $l \leq 5$), 5pnl ($n \leq 10$ for $l \leq 1$, $n \leq 8$ for $l \leq 4$, $n \leq 7$ for $l = 5$), 5s ²
Sr	II	4p⁶5s , 4p⁶4d , 4p⁶5p , 4p⁶4f , 4p ⁶ nl ($n \leq 8$ for $l \leq 3$, $n \leq 6$ for $l \leq 5$), 4p ⁵ 5snl ($n \leq 8$ for $l \leq 2$, $n \leq 6$ for $l \leq 5$), 4p ⁵ 5s ² , 4p ⁵ 4d ² , 4p ⁵ 5p ² , 4p ⁵ 4f ²
Sr	III	4s²4p⁶ , 4p ⁵ 4s ² nl ($n \leq 10$ for $l \leq 2$, $n \leq 8$ for $l \leq 5$), 4p ⁴ 4s ² nl ² ($n \leq 10$ for $l \leq 2$, $n \leq 8$ for $l \leq 5$)
Sr	IV	5s²4p⁵ , 4s4p ⁶ , 4s ² 4p ⁴ nl ($n \leq 10$ for $l \leq 2$, $n \leq 8$ for $l \leq 5$), 4s ¹ 4p ⁵ nl ($n \leq 10$ for $l < 2$, $n = 13$ for $l = 2$, $n \leq 8$ for $l \leq 5$)
Y	I	4d5s² , 4d²5s , 4d5s5p , 5s²5p , 5s ² 6p, 4d5snl ($n \leq 10$ for $l \leq 2$, $n \leq 8$ for $l \leq 5$), 4d ² nl ($n \leq 10$ for $l \leq 2$, $n \leq 8$ for $l \leq 5$), 4d ³ , 5s ² 5d, 5s ² 7s, 5p ² 4d
Y	II	5s² , 4d² , 4d5s , 4d5p, 5snl ($n \leq 10$ for $l \leq 2$, $n \leq 8$ for $l \leq 5$) 4dnl ($n \leq 10$ for $l < 2$, $n \leq 8$ for $l \leq 5$)
Y	III	4p⁶4d , 4p⁶5s , 4p⁶5p , 4p⁶4f , 4p ⁶ nl ($n \leq 8$ for $l \leq 3$, $n \leq 6$ for $l \leq 5$), 4p ⁵ 5snl ($n \leq 8$ for $l \leq 3$, $n \leq 6$ for $l \leq 5$), 4p ⁵ 5s ² , 4p ⁵ 4d ² , 4p ⁵ 5p ² , 4p ⁵ 4f ²
Y	IV	4p⁶ , 4p ⁵ nl ($n \leq 10$ for $l \leq 2$, $n \leq 8$ for $l \leq 5$)
Zr	I	4d²5s² , 4d³5s , 4d²5s5p , 4d ² 5p ² , 4d5s ² 5p, 4d5s5p ² , 4d5p ³ , 4d ⁴ , 4d ³ nl ($n \leq 10$ for $l \leq 2$), 4d ² 5snl ($n \leq 10$ for $l = 0$, $n \leq 9$ for $l \leq 5$)
Zr	II	4d²5s , 4d5s² , 4d²5p , 4d5p² , 4d5s5p , 4d³ , 4d5snl ($n \leq 10$ for $l \leq 2$, $n \leq 8$ for $l \leq 5$)
Zr	III	4d² , 5p ² , 4dnl ($n \leq 10$ for $l \leq 2$, $n \leq 8$ for $l \leq 5$), 5snl ($n \leq 8$ for $l \leq 2$, $n \leq 6$ for $l \leq 5$)
Zr	IV	4d , nl ($n \leq 8$ for $l \leq 5$)

(Bar-Shalom et al. 2001; Tanaka et al. 2018; Banerjee et al. 2022, 2024). Hence, we only briefly summarize some of the key theoretical aspects of this code here.

HULLAC calculates a set of fully relativistic orbitals to determine the energy levels and radiative transition probabilities. The main theoretical framework of HULLAC revolves around using the first order perturbation theory with a central field potential, which includes both nuclear field and the spherically averaged electron-electron interaction. The zero order orbitals are the solution of the single electron Dirac equation. HULLAC uses parametrized central field potential. The free parameter of the distribution is determined by the minimization of the first-order configuration averaged energies for the selected configurations. For the continuum orbitals, the

phase amplitude equation is solved for the parametric potential for the bound electrons with an asymptotic correction.

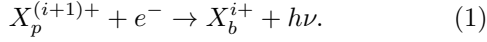
2.2. Method

We use the *level mode* of HULLAC to perform the calculations of the recombination cross sections. The configurations used for the HULLAC calculations are listed in Table 1. Below we discuss in more detail the calculations for rates of direct RR, resonant DR, and PI cross-sections. Note that we do not focus extensively on optimizing the atomic data, as our primary goal is to investigate how the detailed recombination rate coefficients and photo-ionization cross-sections will modify the kilonova nebular spectra, when used, in compari-

son to the constant rates used before (Pognan et al. 2023). Further optimization and fine tuning of the data is within the scope of the future work.

2.2.1. Radiative recombination

The direct process of recombination, RR, occurs when an electron collides with an ion and recombines to a bound state, resulting in the emission of a photon. This process can be described as

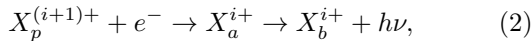


Here p and b represents the parent state of recombining ion and bound state of recombined ions. The energy of the emitted photon corresponds to the sum of the binding energy of the electron and its initial kinetic energy. Since there are no constraints on the kinetic energy of the electron, it is a non-resonant process.

HULLAC calculates the radiative recombination rates by obtaining the relativistic dipole transitions between a bound and a continuum level with the condition that the total energy of the continuum level involved is higher than the bound level. The RR cross-sections are provided as a function of the electron energy, which are then convolved with the Maxwell-Boltzmann velocity distribution for a given temperature to get the RR rates in $\text{cm}^3 \text{s}^{-1}$. Note that our calculations assume the transitions involving only the ground states of the consecutive ions. For light ($Z = 1 - 26$) elements that channel typically makes up $\sim 5 - 20\%$ of the total recombination rate - as such the total rate needed in the NLTE calculations should be multiplied by a factor of ~ 10 .

2.2.2. Dielectronic recombination

The other route via which recombination occurs is DR, which is a resonant process. In this case, the kinetic energy of the free electron excites a bound electron to move to a bound excited state, and in the process, produces a short lived doubly excited autoionizing state. The doubly excited system either autoionizes back to the original configuration, or decays to form a (recombined) singly excited bound state. If the second process occurs, the DR process has occurred. Since the energy of the electron must be the same as the energy difference between the two states $X_p^{(i+1)+}$ and X_a^{i+} , this is a resonant process. This two-step resonant DR process can be written as:



where a represents the autoionizing state.

DR rate coefficients can be determined as the dielectronic capture rate times the fraction that decays into bound states (branching ratio). Assuming the DR is dominated by the population in the ground level of the

recombining ion ($X_p^{(i+1)+}$), the DR rate through autoionization state a is calculated as (Burgess 1964; Nussbaumer & Storey 1983):

$$\alpha_{\text{DR}}(p, a, T_e) = \frac{N_S(X_a^{i+})}{N_e N_S(X_p^{(i+1)+})} \frac{\sum_j A_{aj} \sum_c \Gamma_{ac}}{\sum_c \Gamma_{ac} + \sum_k A_{ak}}, \quad (3)$$

where N_S is the number density at thermo-dynamic equilibrium with N_e being the electron number density. A_{aj} is the radiative transition rate from state a to the bound state j , A_{aL} is the radiative transition rate from state a to the bound state L , Γ_{ac} is the autoionization rate between the autoionizing state a and the continuum state c , and the level population term is given as (Burgess 1964; Nussbaumer & Storey 1983)

$$\frac{N_S(X_a^{i+})}{N_e N_S(X_p^{(i+1)+})} = \frac{g_a}{2g_p} \left(\frac{h^2}{2\pi m_e k T_e} \right)^{3/2} e^{-E_{\text{th}}/k T_e}. \quad (4)$$

Here g_a and g_p are the statistical weights of the autoionizing state a and the ground state p of the recombining ion, E_{th} is the threshold energy between the autoionization state and the higher ion state, and the other symbols have their usual meaning. The j -summation in Equation (3) is over all the levels that are stable against autoionization, whereas the k -summation is over all the lower levels. The c -summation is over all the energetically accessible continuum levels. Finally the total DR rate coefficient is calculated by the summation over the individual autoionizing levels.

At nebular temperatures, in the low density plasma of the kilonova ejecta, mainly the ground term and the first few excited states of the ions are significantly populated. Hence, the autoionizing states only slightly above the ionization threshold can significantly contribute to recombination. Therefore, we choose to resolve the energy levels within 2 eV of the ionization threshold for our calculation.

2.2.3. Photoionization cross sections

PI processes are the inverse of the recombination process. It is possible to have both direct and resonant PI, corresponding to the direct RR and resonant DR process, respectively. Here we calculate only the direct PI cross-sections, using detailed balance. Note that we compute the PI cross-sections for the ground-to-ground transitions only. For the higher excited states, we use hydrogenic cross-sections in our radiative transfer simulations.

3. ATOMIC CALCULATION RESULTS

In Figure 1, we compare the ionization threshold energies obtained from HULLAC to those provided in the

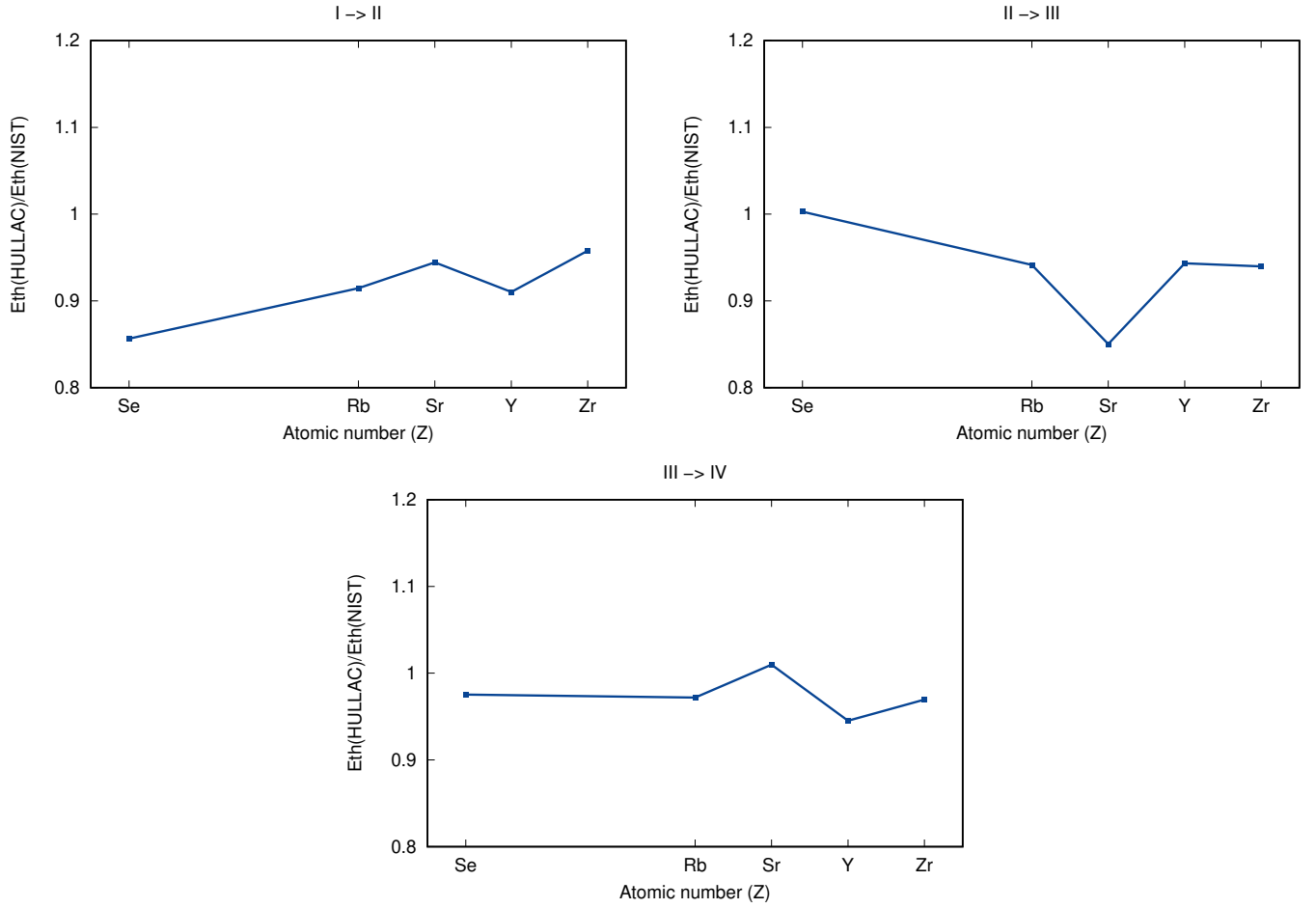


Figure 1. The ratio between the (ground state) ionization threshold energies obtained from HULLAC to those provided in the NIST database (Kramida et al. 2020). The results show good agreement across all the different elements considered.

NIST database (Kramida et al. 2020). This comparison serves as an indication of the overall accuracies of the HULLAC results. The HULLAC results show overall good agreement ($\sim 5\%$) with NIST values across the different ions considered. The differences are relatively larger for Se I and Sr II ($\sim 15\%$), which is likely attributable to the complex electronic structures of these ions. For instance, neutral and singly ionized Se (Se I and II) have the nearly half-filled $4p$ -shell in their ground configurations ($4s^2 4p^4$ and $4s^2 4p^3$ for Se I and II, respectively). Likewise, singly and doubly ionized Sr (Sr II and III) have the completely filled $4p$ -shell ($5s 4p^6$ and $4p^6$ for Sr II and III, respectively) in the ground configuration. The agreement improves for higher ionized species considered, as the electronic configurations becomes relatively simpler. Take for example, the match between the ionization thresholds approaches near unity for the transitions from the ionization state of III to IV.

3.1. Radiative recombination rates

The RR rate coefficients are shown in Figure 2. The values span a wide range of values, from 10^{-15} to $10^{-9} \text{ cm}^3 \text{ s}^{-1}$, depending on the ion species. The RR rates are generally higher for Se and Rb ions. Previous studies, such as Hotokezaka et al. (2021), use analytical approximations of RR rates for Fe ($Z = 26$) from Axelrod (1980), assuming these rates are similar to the rates for the heavier elements as well. To check the accuracy of this assumption, we overplot these analytical rates (black curves in Figure 2) with our detailed calculations. We find that the detailed rates vary significantly across the temperatures in comparison to these analytical values. This suggests that the use of detailed rates will likely influence the spectral calculations.

3.2. Dielectronic recombination rates

Figure 3 shows the DR rate coefficients (in $\text{cm}^3 \text{ s}^{-1}$) for various ions as a function of temperature. Note that we show DR rate coefficients for the temperature range only between $T = 1,000 - 30,000 \text{ K}$. This is because the temperature in the nebular phase typically lies around

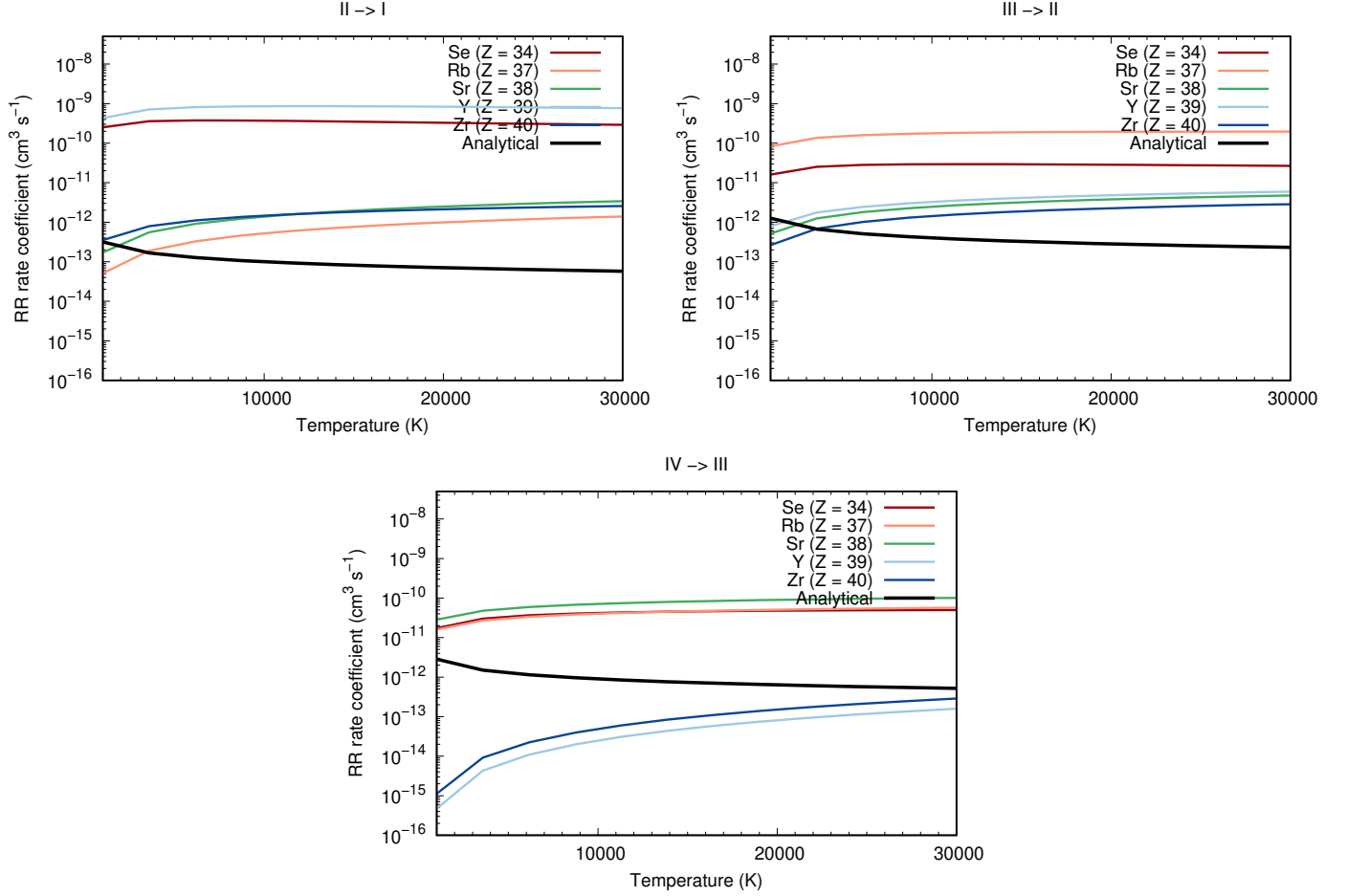


Figure 2. The radiative recombination (RR) rates (to ground state) as a function of temperatures for different elements. The different panels represent different recombination stages (upper left: II to I, upper right: III to II, bottom: IV to III). The same for Fe calculated using analytical method by [Axelrod \(1980\)](#) is plotted for comparison.

$T \sim 10,000$ K (up to \sim first few weeks, [Pognan et al. 2022a](#)), and can be increased up to $\sim 30,000$ K (at around $t = 100$ days, depending on the ejecta composition [Pognan et al. 2022a](#)).

The dielectronic recombination (DR) rates for different ions considered shows different trend with temperature. For ease of understanding, we first discuss the DR rates of the ions Rb ($Z = 37$) II and Y ($Z = 39$) II (Figure 3). For Rb II, the DR rate is negligible at temperatures $T < 15,000$ K, beyond which, the value reaches about $\sim 5 \times 10^{-14} \text{ cm}^3 \text{ s}^{-1}$ at $T \sim 30,000$ K. On the other hand, for Y II, the DR rate shows a high value of $\sim 5 \times 10^{-10} \text{ cm}^3 \text{ s}^{-1}$ at $T \sim 1,000$ K. At the higher temperature of up to $T = 10,000$ K, the DR rate shows an overall decreasing trend. The other ions show similar, or combinations of, such trends with temperatures.

The DR rates are determined both by the dielectronic capture rates and the fraction (branching ratio) that radiatively stabilize. To understand whether dielectronic capture is possible at a certain temperature, we plot the

distribution of energy levels (Figure 4). We also show the threshold energy to provide the idea about the autoionizing energy levels (Figure 4). For Rb I, there are two distinct distribution of the energy levels, peaking at $E \sim 4$ eV and at $E \sim 21$ eV. However, the autoionization levels of Rb I lies at relatively high energies ($E > 16$ eV). On the other hand, Y I has a relatively dense distribution of energy levels spanning the energy range of $E < 10$ eV.

Since the autoionizing levels of Rb I lies at relatively high energies, the level populations in the autoionization levels are negligible at low temperatures. This explains the negligible DR rates of Rb II at lower temperatures. Since the autoionization levels start becoming populated at relatively high temperatures, there is a gradual increase in the DR rate. On the contrary, the autoionizing levels of Y I lie at relatively low energies, which makes it easier to populate them even at low temperatures. Hence, the value of the DR rate for Y II to Y I recombination is high already at low temperatures. We

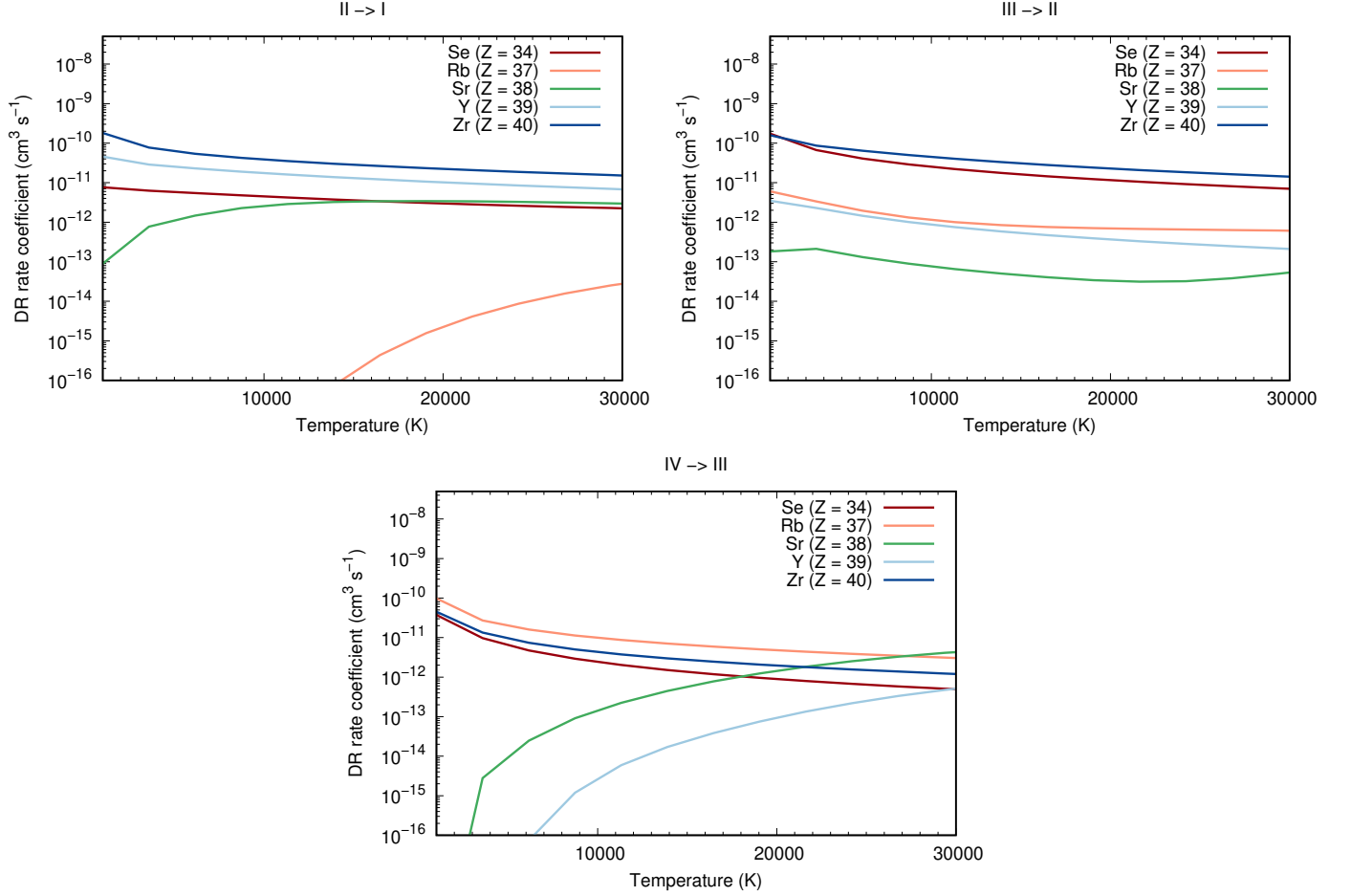


Figure 3. The dielectronic recombination (DR) rates as function of temperature for the different elements. The different panels represent different recombination stages (upper left: II to I, upper right: III to II, bottom: IV to III).

see a slightly decreasing trend following the trailing tail of the Boltzmann distribution.

The values of the DR rates are also quite different between the two ions at all temperatures considered. Going back to our examples, at a temperature of $T = 20,000$ K, the difference in the DR rates between Rb II and Y II are almost 3 orders of magnitudes, with Y having the higher value. This is because the energy level density is relatively high for the Y I, due to the presence of the $4d$ -shell. Also, the autoionization levels are low-lying. Hence, the number of transitions possible to radiatively stabilize from autoionization levels are relatively higher (Figure 5).

The variations in the DR coefficients in the other ions can be understood in the similar way. Around the temperature $T = 10,000$ K, DR rate coefficients for recombining from the ionization state of II to I vary between $10^{-12} - 5 \times 10^{-11} \text{ cm}^3 \text{ s}^{-1}$ for different elements considered. For recombination from the ionization state III to II the range spanned is $10^{-13} - 5 \times 10^{-11} \text{ cm}^3 \text{ s}^{-1}$, and for IV to III it is $2 \times 10^{-15} - 10^{-11} \text{ cm}^3 \text{ s}^{-1}$. One noteworthy

result is that out of the different elements across different ionizations, Zr (navy blue curve in Figure 3) shows relatively higher values for almost the whole temperature range considered. This is because Zr has a dense energy level structure (not shown) for both the recombining and the recombined ion due to the presence of the $4d$ -shell in its ground state. Also, the autoionizing levels are relatively low-lying in this case, making it possible to populate at relatively lower temperatures.

3.3. Total recombination rate

The total rate coefficients, which include both RR and DR contributions, range from 10^{-15} to $10^{-9} \text{ cm}^3 \text{ s}^{-1}$ for the different ions (Figure 6). In most of the cases, these rates are not constant, especially at lower temperatures ($T < 10,000$ K), contrary to assumptions of a temperature-independent value of $10^{-11} \text{ cm}^3 \text{ s}^{-1}$ used in earlier spectral calculations (Pognan et al. 2023). This assumption might affect the spectral models from previous works, an issue we will examine in more detail in the next section.

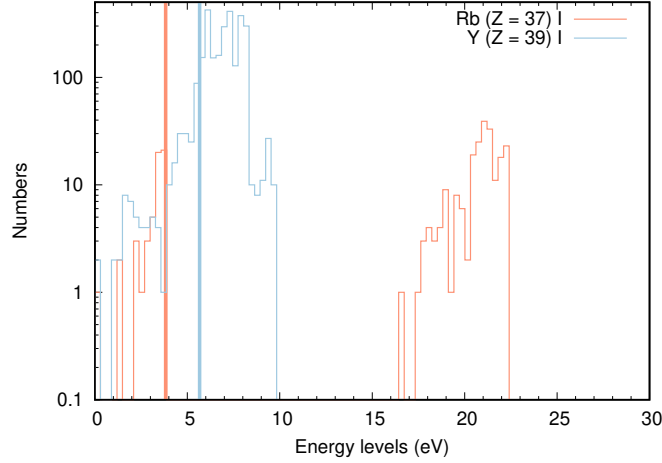


Figure 4. Distribution of energy levels of Rb I and Y I. The autoionizing levels (right) are beyond the ionization threshold.

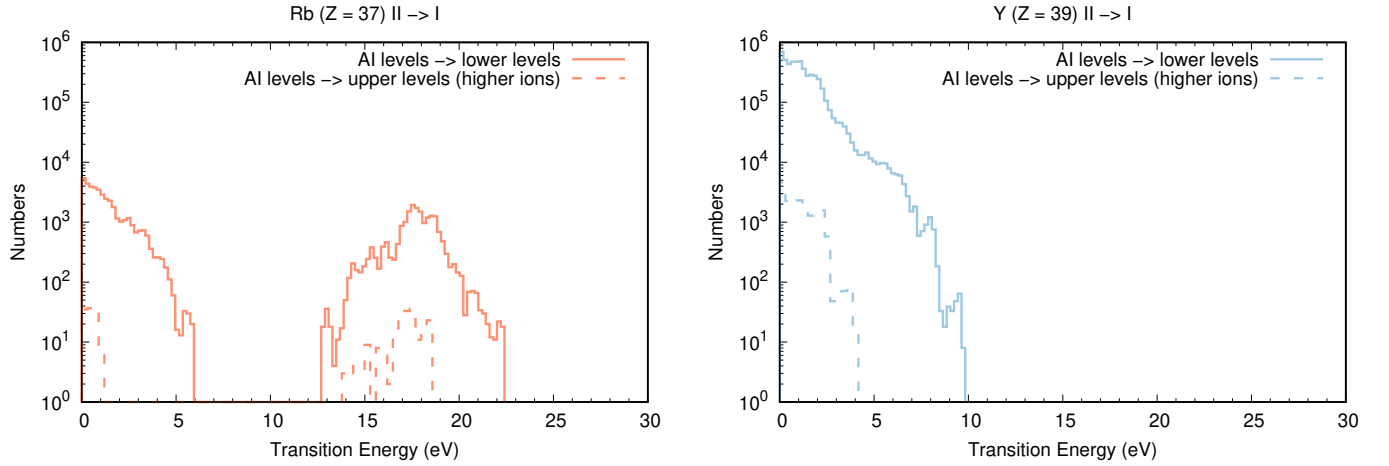


Figure 5. The transitions from the autoionization levels to the lower levels for Rb I (left) and Y I (right).

In Figure 7, we summarize the total rate coefficients for various ions over a temperature range of $T = 1,000$ to $11,000$ K, which is crucial for understanding kilo-nova nebulae a few weeks after the event (Pognan et al. 2023). For transitions from singly ionized to neutral ions (II to I), Se, Y, and Zr has the highest total rates for the recombination (ranging between $\sim 10^{-9} \text{ cm}^3 \text{ s}^{-1}$ to $\sim 10^{-10} \text{ cm}^3 \text{ s}^{-1}$), while Rb has the smallest ($\sim 10^{-13} - 10^{-12} \text{ cm}^3 \text{ s}^{-1}$). For doubly to singly ionized recombination (III to II), Se, Rb, and Zr exhibit the highest recombination rates ($\sim 10^{-10} \text{ cm}^3 \text{ s}^{-1}$), whereas Sr and Y show lower values ($\sim 10^{-12} - 10^{-11} \text{ cm}^3 \text{ s}^{-1}$). Finally, for triply to doubly ionized recombination (IV to III), the different ion species considered show similar values of $\sim 10^{-11} - 10^{-10} \text{ cm}^3 \text{ s}^{-1}$, except for Y, which shows a lower value of $\sim 10^{-15} - 10^{-13} \text{ cm}^3 \text{ s}^{-1}$.

3.4. Photoionization cross sections

We calculate the PI cross-section from the RR cross sections using the Milne relations. We then fit the PI cross sections as a function of incident photon energy using a broken power law. The coefficients for the fitting are provided in Table 2. Note that we consider the cross-section only from ground to ground transitions for the consecutive ions.

3.5. Comparison to previous works

To ensure the reliability of our results, it is important to benchmark the atomic calculation results with other works. Unfortunately, for the heavier elements the availabilities for the atomic data are limited. Hence, to get an idea of the uncertainties existing in our calculations, we compare with the recombination coefficients calculated for Se ionized to I - III by Sterling & Witthoeft (2011) using AUTOSTRUCTURE (Badnell 1986; Badnell et al. 1997).

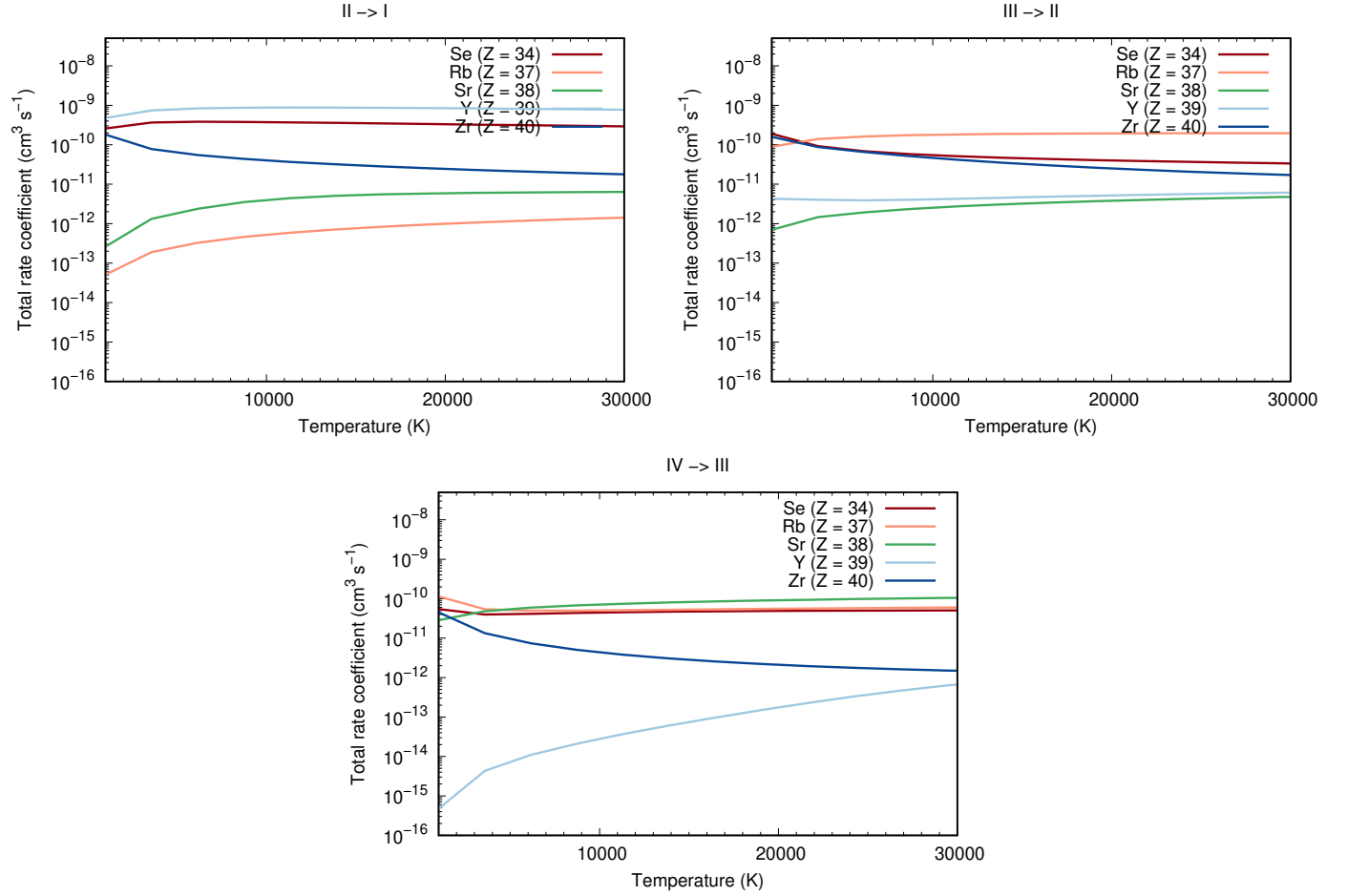


Figure 6. The total recombination rates (DR total plus RR ground state) as function of temperature. The different panels represent different recombination stages (upper left: II to I, upper right: III to II, bottom: IV to III).

For the RR coefficients, the differences between different Se ions vary from $\sim 1 - 2$ orders of magnitude, the match being worse for lower ions due to their more complicated structures. The differences most probably stems from the fact that the RR coefficients are sensitive to the configuration sets used for calculation, which are not tuned between the two calculations. For the DR coefficients, the differences between different ions Se are much smaller, at a maximum within factor of 3 for Se III \rightarrow II. The DR cross-sections are sensitive to the near threshold energy level structures, which are not tuned between the two calculations.

Although there are differences when the RR and DR rates are considered individually, comparison of the total recombination rates show a reasonable match for all the ions. For example, the match between the total coefficients of the ions Se II \rightarrow I, III \rightarrow II, and IV \rightarrow III are within factors of ~ 10 , 2, and 1.5 respectively. The deviation is slightly larger for neutral Se due to its complicated structure. In our radiative transfer calculations, we use the total recombination rates, hence, the overall

degree of uncertainty propagating into the spectral calculations is indicated by these numbers. A more detailed discussion about the differences between the recombination coefficients between HULLAC and AUTOSTRUCTURE calculations will be done in an upcoming paper.

4. RADIATIVE TRANSFER CALCULATION

To study the impact of the new atomic data, we compute kilonova spectra in the NLTE phase ($\gtrsim 10$ d) using the spectral synthesis code SUMO (Jerkstrand et al. 2011). The details of modelling kilonova at NLTE phase has been discussed in the previous works (see Pognan et al. 2023), and hence, we only provide brief essence of the modelling in Appendix A.

We consider the ejecta with a total mass of $0.05 M_{\odot}$ and a power law density profile with an index $n = 4$ similar to that of the polar dynamic ejecta in (Kawaguchi et al. 2020), distributed within the velocity range of $v_{ej} = 0.05c - 0.3c$. We divide the ejecta into five radial zones, spaced linearly with a velocity step of $v_{step} = 0.05c$.

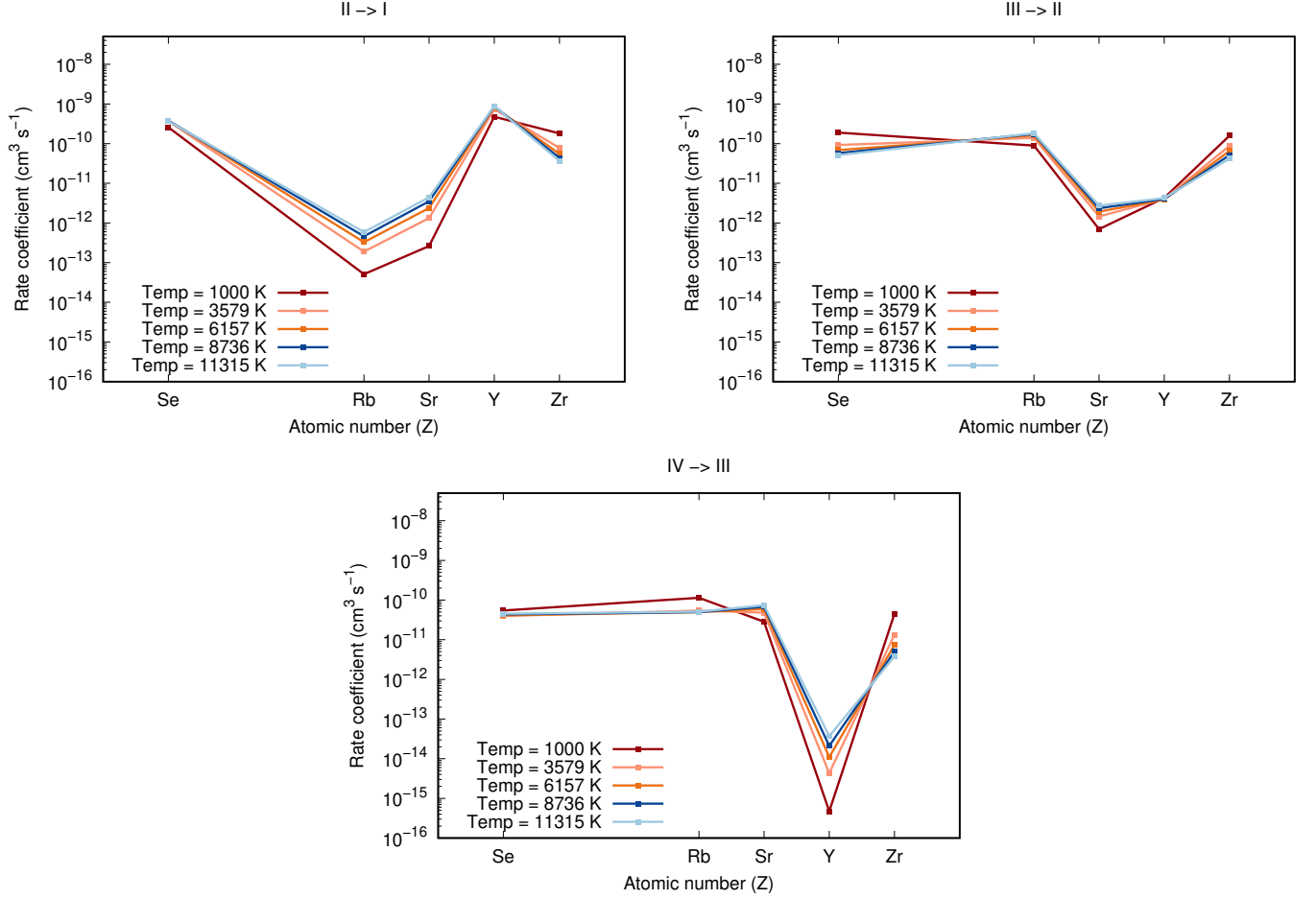


Figure 7. The total recombination rates (DR + RR ground) for different ions at five different temperatures. The different panels represent different recombination stages (upper left: II to I, upper right: III to II, bottom: IV to III).

We use a light r -process composition, with abundances based on the $Y_e = 0.35$ trajectory of [Wanajo et al. \(2014\)](#), limiting the composition to the ten elements in the $Z = 31 - 40$ range (which make up $\gtrsim 80\%$ of the mass and provides most contribution to the spectra, [Pognan et al. 2024](#)). We use the radioactive decay and thermalization physics described in [Kasen & Barnes 2019](#). We use a default collision strength of 10 times the [Axelrod \(1980\)](#) value to improve consistency with new r -process calculations ([Bromley et al. 2023](#)). We compute the spectra at $t = 10$ days and $t = 25$ days, under the steady state approximation.

For the atomic data related to the ionization structure solutions, we use the total recombinations rates and PI cross-sections for the selected elements ($Z = 34, 37 - 40$) as calculated in this work and described in [Section 3](#). To compensate for the fact that our RR rates consider the transitions between the ground states of the consecutive ions only, we multiply the total RR rate by a factor of 10. Furthermore, we assume that the PI cross-section for the whole ground term ([Kramida et al. 2020](#)) is the same as

that of the ground level. Cross sections for other excited states are treated in the hydrogenic approximation.

We refer to the model using the new recombination rates and PI cross sections as the *new* model. We also calculate one model using, as in [Pognan et al. 2024](#), constant recombination rates and hydrogenic PI cross sections. We refer to this model as the *old* model.

For the rest of the atomic data, we mostly follow the treatment in [Pognan et al. 2023](#). However, we update the energy levels of a few low-lying states in selected ions of particular importance, retrieving experimentally verified energy levels from NIST ([Kramida et al. 2020](#)). For Se I, we update the energies of levels 2-5, for Se II levels 2-5, for Se III levels 2-5, for Se IV level 2, with all Se data from [Moore \(1971\)](#). For Y I, level 2 ([Palmer 1977](#)) is updated. Finally for Y II and Zr III, levels 2-12 ([Nilsson et al. 1991](#)) and levels 2-8 ([Reader & Acquista 1997](#)) are updated.

Some commenting is warranted regarding the treatment of bound-free (BF) emission. In detail, RR is associated with a BF emission governed by the specific cap-

Table 2. Fits to photo-ionization cross-sections for different ions.

Element	Ion	σ (cm ²)	β	σ' (cm ²)	β'	E_{br} (eV)
Se	II	9.64×10^{-14}	30.22	9.52×10^{-14}	-2.32	9.03
Se	III	4.79×10^{-16}	48.61	4.83×10^{-16}	-2.16	22.33
Se	IV	4.12×10^{-15}	32.85	4.56×10^{-15}	-1.72	33.27
Rb	II	7.93×10^{-16}	1.931	7.67×10^{-16}	-1.41	12.65
Rb	III	4.58×10^{-14}	22.95	4.58×10^{-14}	-1.69	28.21
Rb	IV	2.67×10^{-15}	15.61	2.94×10^{-15}	-1.33	43.75
Sr	II	6.01×10^{-15}	3.497	6.63×10^{-15}	-1.3	11.83
Sr	III	6.33×10^{-16}	14.91	1.33×10^{-15}	-1.34	11.58
Sr	IV	1.28×10^{-14}	19.07	1.35×10^{-14}	-1.19	48.86
Y	II	1.58×10^{-13}	6.041	1.58×10^{-13}	-2.69	7.57
Y	III	2.42×10^{-15}	6.569	2.87×10^{-15}	-1.43	16.99
Y	IV	1.4×10^{-17}	18.4	3.35×10^{-17}	-0.08	26.77
Zr	II	6.68×10^{-16}	9.201	1.99×10^{-15}	-1.5	8.15
Zr	III	1.15×10^{-15}	6.208	1.24×10^{-15}	-1.49	19.08
Zr	IV	4.57×10^{-17}	18.80	1.63×10^{-16}	-0.08	29.59

ture cross-section as function of electron energy. SUMO however does not treat BF emission in that level of detail, as typically only the RR rates (velocity-integrated cross sections) are entered in the atomic data library. The BF emissivity is therefore approximated as a flat emissivity over energies $\chi_i + 1/2kT$ to $\chi_i + 3/2kT$, for recombination to level i , where χ_i is the ionization potential (Jerkstrand et al. 2011).

For dielectronic recombination, the bound-free emissivity is a delta-function ("lines") at energy $\chi_i + a_j$, where a_j is the energy of autoionizing state j . However, summing this up over all AI states will give a set of BF lines covering a similar energy range (as only these can be accessed by the thermal electrons). As such, the same treatment is done as for RR, with a flat continuum emissivity. It is probably doubtful that the accuracy of the specific energies of the AI states is good enough that a more detailed treatment would be meaningful.

4.1. Spectra at $t = 10$ days

Figure 8 compares the ionization and temperature structures using the old and new recombination rates and photoionization cross sections, at $t = 10$ days. Figure 10 shows detailed ionization structures for the elements with new recombination rates. The new model is less ionized, with a factor 1.3 – 2 lower electron fraction, with the difference between the old and new model increasing with velocity coordinate. In the old model,

the most important electron donors (zone 2¹) are Sr III (19%), Kr II (11%), Kr III (9%), and Zr III (8%), whereas the new model has leading contributions by Sr III (40%), Rb II (12%), Kr II (11%) and Y IV (9%). This result is summarised in Table 3. The overall lower ionization in the new model is a consequence of the new recombination rates more often being higher, than lower, than the canonical $10^{-11} \text{ cm}^3 \text{ s}^{-1}$ used in the old model (Figure 6).

The temperatures decrease significantly in the new model, by ~ 700 K in the innermost zone and by over 1200 K in the outermost. For constant ionic cooling capacity, a lower x_e (as in the new model) would lead to higher temperatures. However, as different r -process ions can have very different cooling capacity (Hotokezaka et al. 2021; Pognan et al. 2022b), this can be offset by the changes in the ionization structure, which is what occurs here. Taking zone 1 as example, the new model has strong cooling by Zr I (60%) and Se I (20%), which are too rare in the old model to be dominant. There, instead higher ions such as Kr II do much of the cooling - and their lower Λ curves lead to higher temperatures. In this way, recombination rates indirectly affect the temperatures in kilonovae.

Figure 11 shows the spectral changes induced by the new atomic data at $t = 10$ days. The new model is more heavily dominated by Zr, with strong Zr I cooling and line blanketing extinguishing all or most of the optical

¹ At $t = 10$ days, 77% and 17% (94% total) of the total radioactive energy deposition occurs in zone 1 and 2 respectively - these two zones are therefore the most important to study physical conditions in to understand the spectral formation.

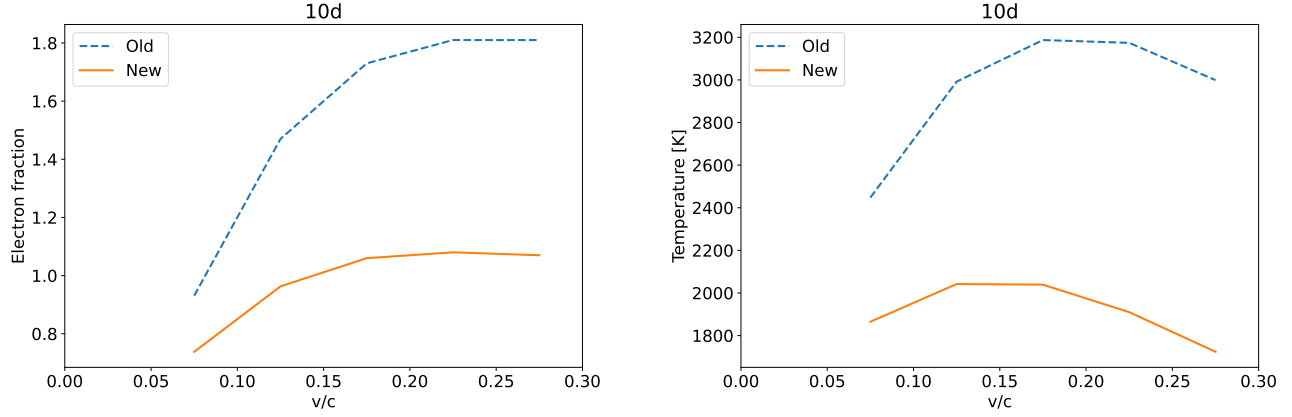


Figure 8. Impact on electron fraction (left) and temperature (right) of using the new recombination rates and photoionization cross sections, at $t = 10$ days.

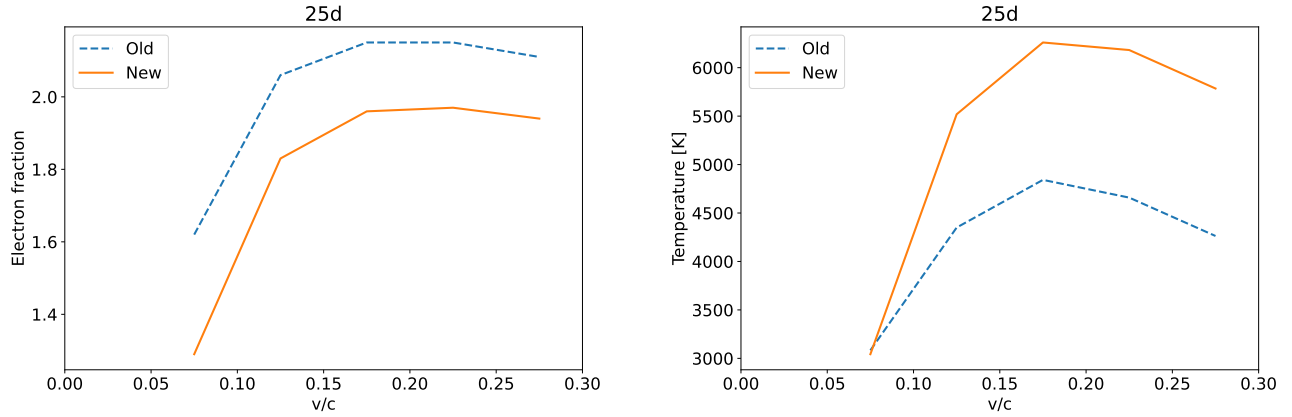


Figure 9. Same as Figure 8, at 25d.

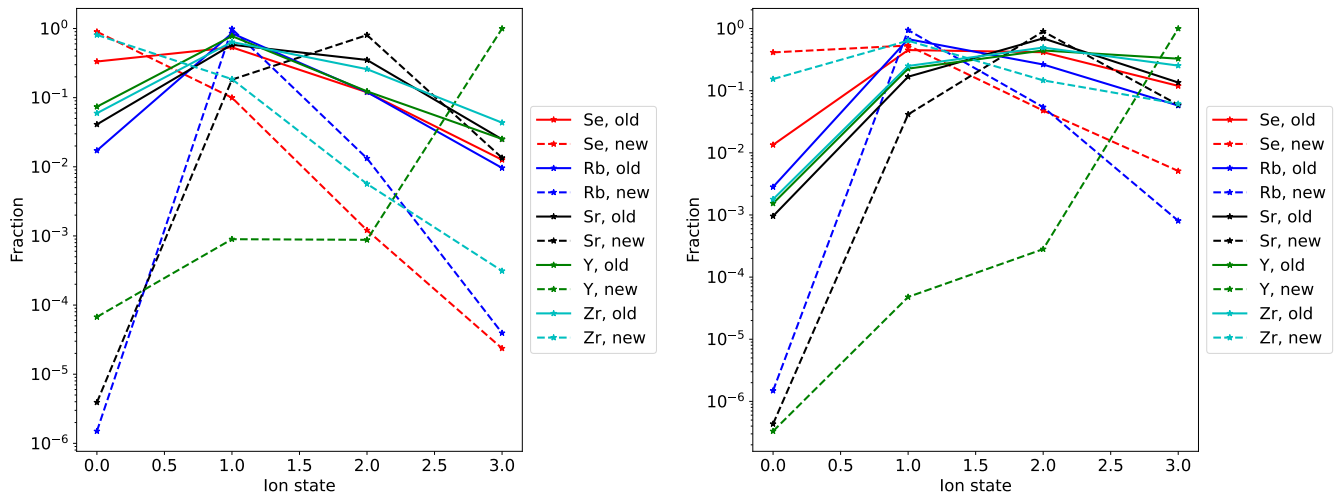


Figure 10. Detailed ionization structure changes (zone 1) for the five elements with new recombination rates, at 10d (left) and 25d (right).

Rb, Y, and Sr flux seen in the old model. The lower temperatures have moved significant power out of the optical/NIR range into the MIR (not plotted), showing that even at $t = 10$ days, the photometric light curves can be significantly affected by the detailed recombination rates.

4.2. Spectra at $t = 25$ days

Figure 9 compares the ionization and temperature structures using the old and new recombination rates and photoionization cross sections at $t = 25$ days. The differences are somewhat smaller at this epoch compared to 10d, with the new rates giving 10–20% lower electron fractions in the different zones, maintaining a similar profile. Looking at the most important electron donors, the old model has leading contributions (zone 2) by Sr III (14%), Kr III (12%), Kr IV (10%), and Zr IV (10%), while the new model maintains the same order but with values 22% (Sr III), 12% (Kr III), 12% (Kr IV) and 12% (Zr IV). Thus, there is in this case a less dramatic change to the ionization structure for the most important electron-donating ions. This picture is further reinforced by Table 3, showing that the overall contributions by different elements to the electron pool changes moderately at 25d. The overall 10–20% reduction is driven by less ionized structures of Se, Rb and Zr, which is not offset by slightly more ionized structures of Kr, Sr, and Y.

Although the temperature in the innermost zone changes little between the models, in zones 2–5 the new model is hotter by over 1000 degrees (right panel, Figure 9). While the lower x_e will drive temperatures up (fewer electron collisions per unit time), the larger effect is likely, as at 10d, the different cooling abilities of different ions. For example, for Zr, the new recombination rates are factors of 5–10 higher than the canonical value. In zone 1, the ionization solution changes from I – II – III – IV = 0.0018 – 0.25 – 0.49 – 0.25 to 0.15 – 0.64 – 0.15 – 0.061. The fact that temperature changes show no correlation with the x_e changes is also consistent with this interpretation. Looking again at zone 2 as an example, in the old model cooling is dominated by Se III, at 23%. In the new model, the abundance of the doubly ionized state of Se has changed from 48% to 30%. The Se III replacement - mainly Se II, is not as good coolant as Se III and the ionization change in selenium therefore contributes to a net heating. Similar changes for the other coolants (each can give a positive or negative net change) together adds up for the total change in temperature. While at $t = 10$ days the net effect led to cooling, here it leads to heating - which way it goes depends on the particular ions involved.

The direct cooling by recombination is unimportant, at $\lesssim 0.1\%$ of the total cooling in all zones both with old and new rates, at both $t = 10$ days and 25d. Similarly is photoelectric heating never competitive with the non-thermal heating by large margins.

Figure 12 shows the spectral changes induced by the new atomic data at $t = 25$ days. The new model is, as at 10d, more heavily dominated by Zr. Zr I an extremely effective line blocking agent even at low abundances and hence, with strong Zr I line blanketing extinguishing all of most of the Rb, Y, and Sr flux seen in the old model.

4.3. Discussion

In this section, we compare our spectral results with a few of the previous works. Note that the epoch of calculations does not match the exact epoch of the previous work. However, we take the closest epoch ($t = 25$ days) for discussion.

In Pognan et al. (2023), the P-Cygni feature at $\lambda = 7500 - 7900 \text{ \AA}$ identified by Sneppen et al. (2023) in spectra at 3–6d (and proposed to be caused by Y II) is proposed to possibly be caused by the Rb I through its [2,3]-1 ground state resonance doublet at 7802, 7949 Å. This feature is analogous to the Na I-D doublet in supernovae which is often optically thick despite sodium being mostly ionized. In our new model at $t = 10$ d, the ionization for Rb I in zone 1 changes from Rb I-II-III-IV = 0.017 – 0.85 – 0.12 – 0.0096 in the old model to $1.5 \times 10^{-6} - 0.99 - 0.013 - 4 \times 10^{-5}$ in the new model. The higher rates for the IV→III and III→II recombinations, ($\sim 10^{-10} \text{ cm}^3\text{s}^{-1}$, Section 3) compared the old canonical value ($10^{-11} \text{ cm}^3\text{s}^{-1}$), leads to switching of III and IV states to the II state. On the other hand, the about two orders-of-magnitudes lower rate for II→I recombination, combined with a quite high ground state photoionization cross section for Rb I (combined with Rb I having relatively sparse metastable structuring so ground state photoionization is important), the neutral Rb abundance plummets to 10^{-6} in the new model, causing Rb I lines to disappear. Neither do contributions by yttrium survive in the new model. With the caveat that the model is at 10d and the signature is most clear at 3–6d in AT2017gfo (Sneppen et al. 2023), this lowers the confidence in identification of either of these elements.

Another noteworthy change is in the Se lines. While analyzing the data for nebular spectra of kilonova AT2017gfo by *Spitzer* Space Telescope, Hotokezaka et al. (2022) proposed that in case the ejecta are dominated by the first peak elements, [Se III] should have a strong emission feature around $\lambda = 4.55 \text{ }\mu\text{m}$. In the old model at $t = 25$ days, [Se III] indeed shows this feature,

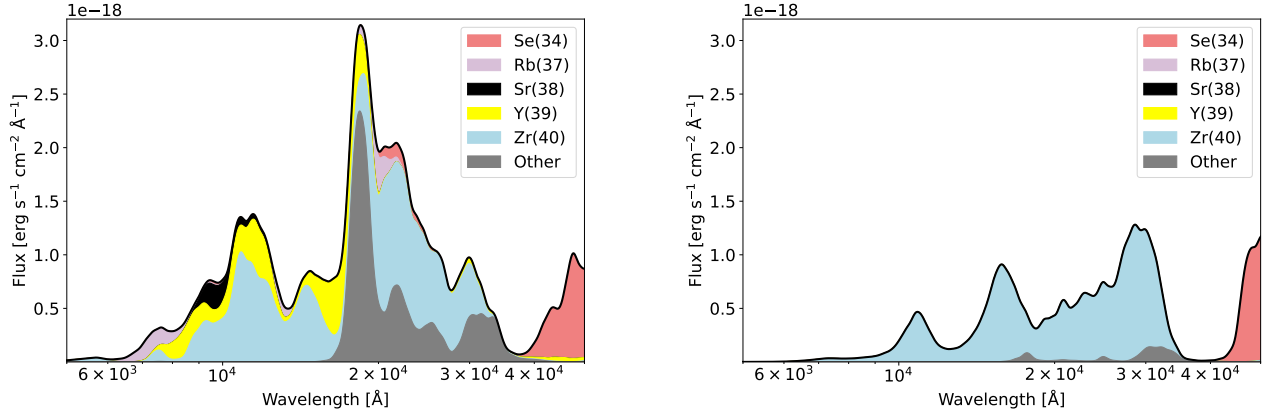


Figure 11. Spectrum at 10d of model using old rates (left) and new rates (right), showing the significant impact of the new recombination rates and photoionization cross sections.

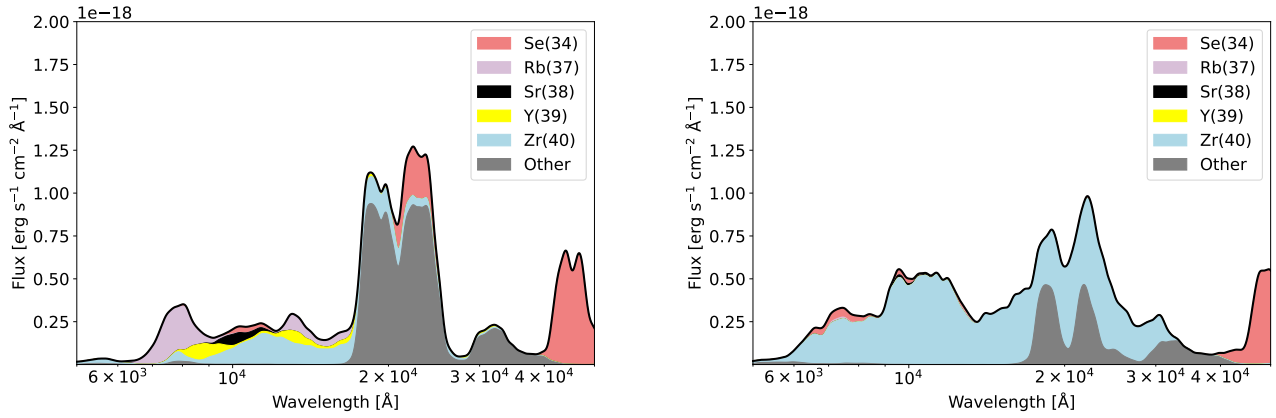


Figure 12. Same as Figure 11, at 25d.

Table 3. Percentage contributions by ions of different elements to the total electron population, in zone 2 at 10d and 25d.

Element	Old($t = 10$ days)	New($t = 10$ days)	Old($t = 25$ days)	New($t = 25$ days)
Ga ($Z = 31$)	0.3	0.4	0.3	0.4
Ge ($Z = 32$)	1.3	1.1	1.2	1.3
As ($Z = 33$)	0.1	0.1	0.1	0.1
Se ($Z = 34$)	14.9	4.1	15.1	11.4
Br ($Z = 35$)	2.5	2.1	2.7	2.8
Kr ($Z = 36$)	22.8	19.5	27.3	28.9
Rb ($Z = 37$)	10.7	12.7	10.2	7.2
Sr ($Z = 38$)	27.6	44.3	24.0	25.1
Zr ($Z = 40$)	15.9	6.4	18.0	15.3

however, in the new model this feature has disappeared. Instead the spectra now has a strong [Se I] line at $\lambda = 5.03 \mu\text{m}$. This is due to the fact that the old model has ionization structure (zone 1) of Se as I – II – III – IV = $0.013 - 0.45 - 0.42 - 0.20$, whereas the new one has a less ionized one at $0.41 - 0.53 - 0.048 - 0.0051$, as the new Se recombination rates are a factor 5-10 higher for all ions compared to the canonical value (Figure 6). In addition to the [Se III] feature, also the [Se IV] line at $\lambda = 2.29 \mu\text{m}$ disappears in the new model.

5. SUMMARY AND CONCLUSIONS

To investigate the nebular phase spectra for kilonova, we perform the necessary detailed atomic calculations. We calculate dielectronic (DR) and radiative (RR) recombination rates, as well as PI cross-sections, for the light r -process elements Se ($Z = 34$), Rb ($Z = 37$), Sr ($Z = 38$), Y ($Z = 39$), and Zr ($Z = 40$). These elements are chosen because they produce potentially strong spectral signatures in light r -process kilonovae (Hotokezaka et al. 2022; Gillanders et al. 2022; Pognan et al. 2023). We consider recombination to ionization states of I – III, as these are most relevant during the nebular phase (e.g., Pognan et al. 2023).

Our results show that around temperature $T = 10,000$ K, DR rate coefficients for recombining from II to I, III to II, and IV to III vary between $10^{-12} - 5 \times 10^{-11} \text{ cm}^3 \text{ s}^{-1}$, $10^{-13} - 5 \times 10^{-11} \text{ cm}^3 \text{ s}^{-1}$ and $2 \times 10^{-15} - 10^{-11} \text{ cm}^3 \text{ s}^{-1}$, respectively, for different elements considered. Furthermore, the RR rate coefficients span a wide range of values, from 10^{-15} to $10^{-9} \text{ cm}^3 \text{ s}^{-1}$, depending on the ion species. This makes the total rate coefficients, which include both RR and DR contributions, range from 10^{-13} to $10^{-9} \text{ cm}^3 \text{ s}^{-1}$ for different ions.

Using the new atomic data, we study the spectra of kilonova at nebular phase using the NLTE spectral synthesis code SUMO (Jerkstrand et al. 2011). We study a model with total ejecta mass $0.05 M_{\odot}$ with a light r -process composition ($Z = 30 - 40$). We calculate the spectra at $t = 10$ days and $t = 25$ days.

The new model shows significant changes in the ionization and temperature profiles, specially at $t = 10$ days, a consequence of the new recombination rates more often being higher than lower the canonical $10^{-11} \text{ cm}^3 \text{ s}^{-1}$ used in the old model. This change in physical condi-

tions significantly changes our spectra at both $t = 10$ and 25 days. We find that the spectra for the new model is more heavily dominated by Zr. Existence of the strong line blanketing by Zr I extinguishes the signatures of most of the Rb, Y, and Sr flux seen in the old model, demonstrating that the capacity to correctly interpret $t \gtrsim 10$ d KN spectra critically depends on accurate recombination rates.

We compare our models with the models in Pognan et al. (2023) and Hotokezaka et al. (2022). With the new recombination rates, we don't obtain the P-Cygni feature at $\lambda = 7500 - 7900 \text{ \AA}$ (Sneppen et al. 2023) proposed by Pognan et al. (2023) to be caused by the Rb I in its [2,3]-1 ground state resonance doublet at 7802, 7949 Å. This occurs because the calculated recombination rate of Rb II \rightarrow I is very low, in combination with an increase of neutral Zr in the ejecta which enhances the line blanketing. Due to a more neutral ionization structure of selenium with the new recombination rates, we don't obtain the [Se III] emission feature at $\lambda = 4.55 \mu\text{m}$, proposed by Hotokezaka et al. (2022), but instead a strong [Se I] $5.03 \mu\text{m}$ line. This shows the importance of the detailed recombination rates for accurate modelling of kilonova spectra at $t \gtrsim 10$ days. If a future kilonova is detected close enough (e.g., within ~ 100 Mpc), observations by the James Webb Space Telescope will provide opportunities to test these Se line predictions.

ACKNOWLEDGMENTS

We acknowledge funding from the European Research Council (ERC) under the European Union's Horizon 2020 Research and Innovation Program (ERC Starting Grant 803189 – SUPERSPEC, PI: Jerkstrand). SB thanks Dr. Daiji Kato from NIFS, Japan for useful discussion regarding HULLAC. JG thanks the Swedish Research Council for the individual starting grant with contract no. 2020-05467. The computations were enabled by resources provided by the National Academic Infrastructure for Supercomputing in Sweden (NAISS), and the Swedish National Infrastructure for Computing (SNIC), at the Paralleldatorcentrum (PDC) Center for High Performance Computing, Royal Institute of Technology (KTH), partially funded by the Swedish Research Council through grant agreements no. 2022-06725 and no. 2018-05973.

REFERENCES

- Abbott, B. P., Abbott, R., Abbott, T. D., et al. 2017, PhRvL, 119, 161101, doi: 10.1103/PhysRevLett.119.161101
- Axelrod, T. S. 1980, Late time optical spectra from the Nickel(56) Model for type I supernovae

- Badnell, N. R. 1986, *Journal of Physics B Atomic Molecular Physics*, 19, 3827, doi: [10.1088/0022-3700/19/22/023](https://doi.org/10.1088/0022-3700/19/22/023)
- Badnell, N. R., Petrini, D., & Stoica, S. 1997, *Journal of Physics B Atomic Molecular Physics*, 30, L665, doi: [10.1088/0953-4075/30/19/006](https://doi.org/10.1088/0953-4075/30/19/006)
- Banerjee, S., Tanaka, M., Kato, D., & Gaigalas, G. 2024, *ApJ*, 968, 64, doi: [10.3847/1538-4357/ad4029](https://doi.org/10.3847/1538-4357/ad4029)
- Banerjee, S., Tanaka, M., Kato, D., et al. 2022, arXiv e-prints, arXiv:2204.06861. <https://arxiv.org/abs/2204.06861>
- Banerjee, S., Tanaka, M., Kawaguchi, K., Kato, D., & Gaigalas, G. 2020, *ApJ*, 901, 29, doi: [10.3847/1538-4357/abae61](https://doi.org/10.3847/1538-4357/abae61)
- Bar-Shalom, A., Klapisch, M., & Oreg, J. 2001, *JQSRT*, 71, 169, doi: [10.1016/S0022-4073\(01\)00066-8](https://doi.org/10.1016/S0022-4073(01)00066-8)
- Bromley, S. J., McCann, M., Loch, S. D., & Ballance, C. P. 2023, *ApJS*, 268, 22, doi: [10.3847/1538-4365/ace5a1](https://doi.org/10.3847/1538-4365/ace5a1)
- Burgess, A. 1964, *ApJ*, 139, 776, doi: [10.1086/147813](https://doi.org/10.1086/147813)
- Coulter, D. A., Foley, R. J., Kilpatrick, C. D., et al. 2017, *Science*, 358, 1556, doi: [10.1126/science.aap9811](https://doi.org/10.1126/science.aap9811)
- Cowperthwaite, P. S., Berger, E., Villar, V. A., et al. 2017, *ApJL*, 848, L17, doi: [10.3847/2041-8213/aa8fc7](https://doi.org/10.3847/2041-8213/aa8fc7)
- Domoto, N., Tanaka, M., Kato, D., et al. 2022, *ApJ*, 939, 8, doi: [10.3847/1538-4357/ac8c36](https://doi.org/10.3847/1538-4357/ac8c36)
- Drout, M. R., Piro, A. L., Shappee, B. J., et al. 2017, *Science*, 358, 1570, doi: [10.1126/science.aaq0049](https://doi.org/10.1126/science.aaq0049)
- Eichler, D., Livio, M., Piran, T., & Schramm, D. N. 1989, *Nature*, 340, 126, doi: [10.1038/340126a0](https://doi.org/10.1038/340126a0)
- Freiburghaus, C., Rosswog, S., & Thielemann, F. K. 1999, *ApJL*, 525, L121, doi: [10.1086/312343](https://doi.org/10.1086/312343)
- Froese Fischer, C., Gaigalas, G., Jönsson, P., & Bieroń, J. 2019, *Computer Physics Communications*, 237, 184, doi: [10.1016/j.cpc.2018.10.032](https://doi.org/10.1016/j.cpc.2018.10.032)
- Gillanders, J. H., Smartt, S. J., Sim, S. A., Bauswein, A., & Goriely, S. 2022, *MNRAS*, 515, 631, doi: [10.1093/mnras/stac1258](https://doi.org/10.1093/mnras/stac1258)
- Gu, M. F. 2008, *Canadian Journal of Physics*, 86, 675, doi: [10.1139/P07-197](https://doi.org/10.1139/P07-197)
- Hotokezaka, K., Tanaka, M., Kato, D., & Gaigalas, G. 2021, *MNRAS*, 506, 5863, doi: [10.1093/mnras/stab1975](https://doi.org/10.1093/mnras/stab1975)
- . 2022, *MNRAS*, 515, L89, doi: [10.1093/mnrasl/slac071](https://doi.org/10.1093/mnrasl/slac071)
- . 2023, *MNRAS*, 526, L155, doi: [10.1093/mnrasl/slac128](https://doi.org/10.1093/mnrasl/slac128)
- Jerkstrand, A., Fransson, C., & Kozma, C. 2011, *A&A*, 530, A45, doi: [10.1051/0004-6361/201015937](https://doi.org/10.1051/0004-6361/201015937)
- Kasen, D., & Barnes, J. 2019, *ApJ*, 876, 128, doi: [10.3847/1538-4357/ab06c2](https://doi.org/10.3847/1538-4357/ab06c2)
- Kasen, D., Metzger, B., Barnes, J., Quataert, E., & Ramirez-Ruiz, E. 2017, *Nature*, 551, 80, doi: [10.1038/nature24453](https://doi.org/10.1038/nature24453)
- Kawaguchi, K., Shibata, M., & Tanaka, M. 2018, *ApJL*, 865, L21, doi: [10.3847/2041-8213/aade02](https://doi.org/10.3847/2041-8213/aade02)
- . 2020, *ApJ*, 889, 171, doi: [10.3847/1538-4357/ab61f6](https://doi.org/10.3847/1538-4357/ab61f6)
- Korobkin, O., Rosswog, S., Arcones, A., & Winteler, C. 2012, *MNRAS*, 426, 1940, doi: [10.1111/j.1365-2966.2012.21859.x](https://doi.org/10.1111/j.1365-2966.2012.21859.x)
- Kramida, A., Yu. Ralchenko, Reader, J., & and NIST ASD Team. 2020, NIST Atomic Spectra Database (ver. 5.8), [Online]. Available: <https://physics.nist.gov/asd> [2021, April 15]. National Institute of Standards and Technology, Gaithersburg, MD.
- Kulkarni, S. R. 2005, arXiv e-prints, astro. <https://arxiv.org/abs/astro-ph/0510256>
- Lattimer, J. M., & Schramm, D. N. 1974, *ApJL*, 192, L145, doi: [10.1086/181612](https://doi.org/10.1086/181612)
- Li, L.-X., & Paczyński, B. 1998, *ApJL*, 507, L59, doi: [10.1086/311680](https://doi.org/10.1086/311680)
- Metzger, B. D., Martínez-Pinedo, G., Darbha, S., et al. 2010, *MNRAS*, 406, 2650, doi: [10.1111/j.1365-2966.2010.16864.x](https://doi.org/10.1111/j.1365-2966.2010.16864.x)
- Moore, C. E. 1971, in *Bulletin of the American Astronomical Society*, Vol. 3, 154–155
- Nilsson, A. E., Johansson, S., & Kurucz, R. L. 1991, *PhyS*, 44, 226, doi: [10.1088/0031-8949/44/3/003](https://doi.org/10.1088/0031-8949/44/3/003)
- Nussbaumer, H., & Storey, P. J. 1983, *A&A*, 126, 75
- Palmer, B. A. 1977, PhD thesis, Purdue University, Indiana
- Perego, A., Radice, D., & Bernuzzi, S. 2017, *ApJL*, 850, L37, doi: [10.3847/2041-8213/aa9ab9](https://doi.org/10.3847/2041-8213/aa9ab9)
- Pognan, Q., Gruner, J., Jerkstrand, A., & Wanajo, S. 2023, *MNRAS*, 526, 5220, doi: [10.1093/mnras/stad3106](https://doi.org/10.1093/mnras/stad3106)
- Pognan, Q., Jerkstrand, A., & Gruner, J. 2022a, *MNRAS*, 510, 3806, doi: [10.1093/mnras/stab3674](https://doi.org/10.1093/mnras/stab3674)
- . 2022b, *MNRAS*, 513, 5174, doi: [10.1093/mnras/stac1253](https://doi.org/10.1093/mnras/stac1253)
- Pognan, Q., Wu, M.-R., Martínez-Pinedo, G., et al. 2024, arXiv e-prints, arXiv:2409.16210, doi: [10.48550/arXiv.2409.16210](https://doi.org/10.48550/arXiv.2409.16210)
- Preval, S. P., Badnell, N. R., & O’Mullane, M. G. 2019, *Journal of Physics B Atomic Molecular Physics*, 52, 025201, doi: [10.1088/1361-6455/aaf3f4](https://doi.org/10.1088/1361-6455/aaf3f4)
- Reader, J., & Acquista, N. 1997, *PhyS*, 55, 310, doi: [10.1088/0031-8949/55/3/009](https://doi.org/10.1088/0031-8949/55/3/009)
- Rosswog, S., Sollerman, J., Feindt, U., et al. 2018, *A&A*, 615, A132, doi: [10.1051/0004-6361/201732117](https://doi.org/10.1051/0004-6361/201732117)
- Shibata, M., Fujibayashi, S., Hotokezaka, K., et al. 2017, *PhRvD*, 96, 123012, doi: [10.1103/PhysRevD.96.123012](https://doi.org/10.1103/PhysRevD.96.123012)
- Smartt, S. J., Chen, T. W., Jerkstrand, A., et al. 2017, *Nature*, 551, 75, doi: [10.1038/nature24303](https://doi.org/10.1038/nature24303)

- Sneppen, A., Watson, D., Gillanders, J. H., & Heintz, K. E. 2023, arXiv e-prints, arXiv:2312.02258, doi: [10.48550/arXiv.2312.02258](https://doi.org/10.48550/arXiv.2312.02258)
- Sterling, N. C. 2011, A&A, 533, A62, doi: [10.1051/0004-6361/201117471](https://doi.org/10.1051/0004-6361/201117471)
- Sterling, N. C., & Witthoeft, M. C. 2011, A&A, 529, A147, doi: [10.1051/0004-6361/201116718](https://doi.org/10.1051/0004-6361/201116718)
- Tanaka, M., Utsumi, Y., Mazzali, P. A., et al. 2017, PASJ, 69, 102, doi: [10.1093/pasj/psx121](https://doi.org/10.1093/pasj/psx121)
- Tanaka, M., Kato, D., Gaigalas, G., et al. 2018, ApJ, 852, 109, doi: [10.3847/1538-4357/aaa0cb](https://doi.org/10.3847/1538-4357/aaa0cb)
- Utsumi, Y., Tanaka, M., Tominaga, N., Yoshida, M., & et al. 2017, PASJ, 69, 101, doi: [10.1093/pasj/psx118](https://doi.org/10.1093/pasj/psx118)
- Valenti, S., Sand, D. J., Yang, S., et al. 2017, ApJL, 848, L24, doi: [10.3847/2041-8213/aa8edf](https://doi.org/10.3847/2041-8213/aa8edf)
- Wanajo, S., Sekiguchi, Y., Nishimura, N., & et al. 2014, ApJL, 789, L39, doi: [10.1088/2041-8205/789/2/L39](https://doi.org/10.1088/2041-8205/789/2/L39)
- Watson, D., Hansen, C. J., Selsing, J., et al. 2019, Nature, 574, 497, doi: [10.1038/s41586-019-1676-3](https://doi.org/10.1038/s41586-019-1676-3)
- Yang, S., Valenti, S., Cappellaro, E., et al. 2017, ApJL, 851, L48, doi: [10.3847/2041-8213/aaa07d](https://doi.org/10.3847/2041-8213/aaa07d)

APPENDIX

A. MODELLING NEBULAR SPECTRA

The main source of energy deposition in the KN ejecta comes from the radioactive decay of the heavy elements. The non-thermal β -decay products, i.e., γ -rays, electrons/positrons (e^\pm), and for heavy compositions also α -particles and fission fragments, generate an ionization cascade that heat, ionize and excite the ejecta via collisional interactions. In the tail phase, the ejecta are transparent to γ -rays, and for light compositions the thermalization mainly comes from the electrons/positrons (e^\pm). Furthermore, we also consider the energy deposition from α -decay, although the same from the fission is ignored. The thermalisation efficiencies for β and α decays are taken from [Kasen & Barnes \(2019\)](#).

Here we want to mention that we consider that the microphysical processes at nebular phase are fast enough to re-emit the entire energy deposited in the ejecta instantaneously, i.e., the kilonova nebula is at steady state condition ([Jerkstrand et al. 2011](#)) throughout the calculations. [Pognan et al. \(2022a\)](#) shows that this is true for most of the neutron star merger ejecta at time $t < 100$ days, except for the extremely low density or the low power condition in the ejecta. At later times ($t > 100$ days), the atomic processes becomes slow and the assumption of the steady state breaks down. However, for our purpose and timescale, assumption of steady state is sufficient.

The energy deposited from radioactive decay also contribute to ionization and excitation. The ionization structure of the elements in the ejecta is determined by using rate equation, under the assumption of NLTE. The equation for the rate of change of the ion abundances ($x_{j,i}$ for an element j in ionization state i) is given as:

$$\frac{dx_{j,i}}{dt} = \Gamma_{j,i-1}x_{j,i-1} - (\Psi_{j,i} + \Gamma_{j,i})x_{j,i} + \Psi_{j,i+1}x_{j,i+1}. \quad (\text{A1})$$

Here $\Gamma_{j,i}$ and $\Psi_{j,i}$ are the total ionization and recombination rate per particle, respectively. At steady state, we can assume the ionization equilibrium condition to satisfy, leading to set the time derivative as zero. Hence, we are left with the simpler equation by balancing the ionization and recombination terms:

$$\Gamma_{j,i-1}x_{j,i-1} = \Psi_{j,i}x_{j,i}. \quad (\text{A2})$$

Note that we assume the ionization occurs via non-thermal electron collisions and photoionization, whereas the recombination occurs by direct radiative or resonant dielectronic processes. The ionization and recombination rates generally depend on the ion abundances, and hence, the equations for determining $x_{j,i}$ are non-linear and they are solved by iteration ([Jerkstrand et al. 2011](#)).

The temperature (T) of the ejecta at the nebular phase is determined by using the first law of thermodynamics ([Jerkstrand et al. 2011](#); [Pognan et al. 2022a](#)):

$$\frac{dT(t)}{dt} = \frac{h(t) - c(t)}{3/2k_B n(t)} - \frac{2T(t)}{t}. \quad (\text{A3})$$

In the equation, the first term represents the net heating per particle, whereas the second term stems from the cooling from adiabatic expansion of the ejecta. Here $n(t)$ is the total thermal particle number density, k_B is the Boltzmann constant, $x_e(t)$ is the electron fraction in the ejecta, $h(t)$ and $c(t)$ are the heating and cooling rates per unit volume. Note that although the ionization cooling should be added as a third term ([Jerkstrand et al. 2011](#)), it is negligible for kilonova nebula ([Pognan et al. 2022a](#)), and thus, we do not include it here.

This equation is further simplified using the steady state approximation. At the steady state of nebular phase, the ejecta get continuously heated by the radioactive decay, as well as get cooled off dominantly by line emission following thermal collisional excitation, recombination, free-free emission, and adiabatic expansion. If the heating and the temperature of the ejecta increase, the line cooling by collisional excitation is also increased. Hence, at steady state, the temperature gets balanced and the thermal equilibrium is established, reducing the equation to the simplified form of $h(t) = c(t)$.

The excitation structure within each ion is calculated by using the detailed balance equation. The fraction of an element j at ionization state i in excitation state $k \neq k'$ (we omit the symbol j for simplicity) is given as ([Jerkstrand](#)

et al. 2011):

$$\begin{aligned}
\frac{dx_{i,k}}{dt} = & \sum_{k'} x_{i-1,k'} \Psi_{i-1,k',i,k} + \sum_{k'} x_{i+1,k'} \Psi_{i+1,k',i,k} \\
& + \sum_{k' \neq k} x_{i,k'} \xi_{k',k} - x_{i,k} \left(\sum_{k' \neq k} \xi_{k,k'} \right. \\
& \left. + \sum_{k' \neq k} \Gamma_{i,k,i+1,k'} + \sum_{k' \neq k} \Psi_{i,k,i-1,k'} \right),
\end{aligned} \tag{A4}$$

where ξ is the internal transition and the other symbols have their usual meaning. The internal transitions can happen via spontaneous emission, stimulated emission, photoabsorptions, and both non-thermal and thermal collisions. Under the steady state approximation, the de-excitation time-scale is shorter in comparison to the evolutionary time. Hence, we set the time derivative term to zero, simplifying the equation.

In summary, the thermodynamic properties of the ejecta during the nebular phase, and consequently the nebular spectra of kilonovae are highly dependent on the accurate modeling of detailed microphysical processes. Therefore, precise atomic cross-sections and rates are essential for understanding these microphysical processes and for subsequent modeling of the nebular spectra of kilonova.